

Local strain analysis of the herringbone reconstruction of Au(111) through atomistic simulations

H. Bulou* and C. Goyhenex

IPCMS-GSI, CNRS UMR7504, 23, Rue du Loess, F-67037 Strasbourg Cedex, France

(Received 23 July 2001; published 2 January 2002)

In this paper, the concept of *local surface mismatch* is introduced and calculated in the framework of the tight-binding second moment approximation. Within this concept, the local surface lattice parameter is calculated, taking into account the bonds of the surface atoms with the bulk ones. It is shown that the local surface lattice parameter depends on the relative range of the repulsive part of the potential with respect to the attractive one: the smaller this latter is, the greater the local surface lattice mismatch is. An illustration of the consequences of this concept is given in the case of the herringbone reconstruction of Au(111). A strong dispersion of the in-plane surface nearest-neighbor distances, spreading from 2.68 Å at the kink positions to 2.86 Å in the fcc regions, is reported. A similar dispersion is observed for the hydrostatic pressures. This dispersion explains the preferential nucleation phenomena on such a reconstructed surface.

DOI: 10.1103/PhysRevB.65.045407

PACS number(s): 81.10.Aj, 68.35.Ct, 71.15.Ap, 71.15.Pd

I. INTRODUCTION

Metallic surfaces are thermodynamically unstable in a cleaved-bulk configuration, and some of them reconstruct into an atomic arrangement different from the bulk one. Such a behavior can be observed for every low-index faces of fcc metals, viz (100), (110), and (111) faces. A common explanation is a change in the interatomic forces in different environments at the surface with respect to the bulk environment due to the reduced number of chemical bonds.¹ Because of the lack of electronic density in the cleaved-bulk configuration, the surface atoms try to get closer, in some cases inducing a global atomic rearrangement of the surface.

Numerous studies were devoted to surface reconstruction phenomena as well from a theoretical point of view as from an experimental one, in particular on fcc(110) surfaces. For this orientation, surface reconstructions were observed for Au,^{5–11} Pt,^{12–17} and Ir.^{18–21} On the other hand, a fcc(111) reconstruction is observed only for Au(111),^{24,56} and, in some specific conditions, for Pt(111),^{2–4} and theoretical studies are less common. This lies in the nature of the fcc(111) reconstruction. Unlike a fcc(110) reconstruction, a fcc(111) reconstruction involves a great number of atoms in numerous inequivalent positions with respect to the underlying plane. For example, a typical supercell of the Au(111) herringbone reconstruction is $70 \times 280 \text{ \AA}^2$.³ *Ab initio* studies, which are common for fcc(110) reconstructions, are impossible in the case of a (111) reconstruction. Therefore, only semiempirical methods, like the effective-medium theory and the two-dimensional Frenkel-Kontorova model, have been used up to now, for example in the case of the Pt(111) (Ref. 22) and the herringbone Au(111) reconstructions.²³ Another important consequence of the great number of atoms involved in the fcc(111) reconstructions is the strong structural inhomogeneity of the surface,²⁴ which is assumed to be at the origin of the preferential nucleation observed for Co,^{25,26} Fe,²⁷ Ni,^{28,29} Rh,^{30,31} or Cu (Ref. 32) on Au(111). To our knowledge, no theoretical structural studies of the inhomogeneous herringbone reconstruction of gold at the atomic level have yet been

published. Thus the purpose of this paper is to present a local strain analysis of the herringbone reconstruction of Au(111) through atomistic simulations performed by means of tight-binding quenched-molecular dynamics. Molecular dynamics is a perfectly adapted tool to describe the surface inhomogeneity, since the atoms are allowed to move along three directions of space. In addition, the chemical nature of the atomic bond is taken into account through the interatomic potentials used to derive the forces acting on the atoms. Finally, semiempirical methods allow one to investigate systems containing a great number of atoms (up to several tens of thousands) which is the case of this particular (111) reconstruction.

In the following, an analytical description of the fcc(111) surface behavior is given in the framework of the tight-binding second-moment approximation (TB-SMA) (Sec. II). Then the concepts described in Sec. II are illustrated by a tight-binding quenched-molecular-dynamic study of the herringbone reconstruction of gold (Sec. III). Local strains and hydrostatic pressures of a Au(111)-reconstructed surface are presented. The link between the preferential adsorption on such a surface and the spatial distribution of the hydrostatic pressure is discussed.

II. DRIVING FORCES OF THE RECONSTRUCTION OF CLOSE-PACKED SURFACES OF METALS WITHIN THE SECOND-MOMENT APPROXIMATION OF TIGHT BINDING THEORY

A. Surface misfit m_s

It is now well established that the ability of a transition-metal surface to reconstruct depends on the surface stress, the surface energy, and the energy cost of dislocation formation.^{33–36} These quantities depend on the surface interatomic equilibrium distance. The latter distance is normally shorter than the bulk distance because of the charge redistribution at the surface.¹ Then the surface interatomic equilibrium distance is a key parameter of the reconstruction phenomena.

We define the *local surface lattice parameter* r_0^S as the distance between surface atoms for which the surface site

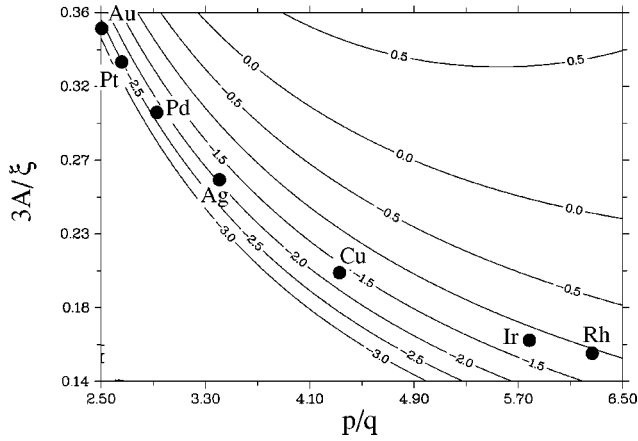


FIG. 1. Contour plot of the variation of the local surface mismatch as a function of p/q and $3A/\xi$. The black dots represent the value for elements quoted in Table I.

energy E^{site} is minimal. The local surface lattice parameter concept is very close to the *effective lattice constant of the surface*, introduced by Dodson in his study of the (001) reconstruction of transition metals.³⁷ However, Dodson's effective lattice constant of a surface was determined from a system where there is no bulk material (2 ML), meaning that the bonding of the surface atoms with underlying bulk atoms is not taken into account. This then induces an overestimation of the surface mismatch. In our model this surface-bulk bonding is considered. Actually, the local surface lattice parameter is similar to the bulk equilibrium distance r_0 , but at the surface.

Note that the calculated local surface lattice parameter, obtained by a minimization of the surface site energy, may differ from the *real* surface lattice parameter. The minimization of the surface site energy does not imply a minimization of the underlying bulk site energy, which can even be slightly increased. The interest of the local surface lattice parameter is to highlight the tendency of the surface lattice in

the cleaved-bulk configuration to contract, which is at the origin of the surface reconstruction of some elements as it will be shown below.

In the framework of the second-moment approximation of the tight-binding theory,³⁸ r_0^S can be determined by minimizing the site energy of surface atoms:

$$E_i^{\text{site}} = E_i^b + E_i^r. \quad (1)$$

E_i^b is the band term, and is obtained by integrating the local density of states up to the Fermi level.³⁸ This gives rise to the many-body character of the potentials necessary to account for surface relaxations and reconstructions.³⁹ When replacing the realistic density of states by a schematic rectangular one having the same second moment, i.e., the same full width at half maximum (*second-moment approximation*⁴⁰), one obtains

$$E_i^b = - \left\{ \sum_{j, r_{ij} < r_c} \xi^2 \exp \left[-2q \left(\frac{r_{ij}}{r_0} - 1 \right) \right] \right\}^{1/2}. \quad (2)$$

Exponent q characterizes the distance dependence of the hopping integral between atoms at sites i and j , ξ is an effective hopping integral, and r_0 is the nearest-neighbor distance in the metal. The interaction is canceled beyond a cutoff radius r_c . The repulsive term E_i^r is described by a sum of Born-Mayer ion-ion repulsion,⁴¹

$$E_i^r = \sum_{j, r_{ij} < r_c} A \exp \left[-p \left(\frac{r_{ij}}{r_c} - 1 \right) \right], \quad (3)$$

where p is related to the bulk modulus of the metal. It is known that the nearest-neighbor interactions are insufficient to reproduce reconstructions.⁴² Hence, in the calculation presented in this paper, the summations in Eqs. (2) and (3) are extended up to the next-nearest neighbors. The qualitative picture of the reconstruction remains unchanged when considering third-nearest neighbors.⁴³ The minimization of Eq. (1) with respect to the distance r between the nearest-neighbor atoms leads to (Cf. the Appendix)

$$m_s = \frac{\delta r}{r_0} \approx (3 + C_q) \frac{\sqrt{3}Ap \sqrt{3 + C_q}(3 + \sqrt{2}C_p) - q\xi(3 + \sqrt{2}C_q)}{[\sqrt{3}Ap^2(3 + C_q)^{3/2}(3 + 2C_p) - 2q^2\xi(3 + 2C_q)(3 + C_q) + q^2\xi(3 + \sqrt{2}C_q)^2]} \quad (4)$$

$$C_q = \exp[-2q(\sqrt{2}-1)], \quad C_p = \exp[-p(\sqrt{2}-1)], \quad (5)$$

where the quantity δr is defined as $\delta r = r_0^B - r_0^S$. Since $C_q \ll 1$ and $C_p \ll 1$,

$$m_s \approx \frac{3Ap - \xi q}{3Ap^2 - \xi q^2}. \quad (6)$$

From Eq. (6), one notes that the surface mismatch depends both on the p/q and $3A/\xi$ ratios. Figure 1 displays a contour plot of the variations of the local surface mismatch as a function of p/q and $3A/\xi$. The most striking point is

that the absolute value of the local surface mismatch is a decreasing function of both ratios. The black dots of this figure represent the values for elements quoted in Table I. The parameters of the TB-SMA potentials used in this calculation are given in Table I. Two observations can be pointed out. The first one is the large variation of the local surface mismatch for the considered elements, from -1% for Rh to -2.75% for Au. The second one is related to the pair of ratios ($p/q, 3A/\xi$): there are two ways to obtain a large surface mismatch. Either one has a small $3A/\xi$ ratio or a small p/q one. In the first case, however, as for Rh and Ir, the effect of a small $3A/\xi$ is counterbalanced by a large p/q ,

TABLE I. Parameters of the model (Ref. 44). * Effective lattice constant of the surface from the Dodson model (Ref. 37).

Element	A (eV)	p	ξ (eV)	q	r_0 (Å)	r_0^S (Å)	m_S (%)	m_S^{Dodson} (%)
Rh	0.094	14.92	1.916	2.380	2.69	2.662	-1.05	-
Ir	0.124	15.98	2.376	2.760	2.71	2.681	-1.07	-
Cu	0.089	10.55	1.280	2.430	2.56	2.513	-1.84	-
Ag	0.103	10.85	1.189	3.180	2.89	2.831	-2.05	-
Pd	0.171	10.90	1.713	3.720	2.75	2.688	-2.27	-
Pt	0.295	10.47	2.693	3.935	2.77	2.709	-2.53	-3.8*
Au	0.210	10.145	1.818	4.03	2.88	2.807	-2.74	-4.3*

inducing a small surface mismatch. Conversely, the elements with a large p/q ratio (Au and Pt, for example) have a large surface mismatch, although $3A/\xi$ is large. This means that the variation of the local surface mismatch is mainly governed by the p/q ratio.

1. Influence of the relative range of the attractive and repulsive parts of the interatomic potential

The p/q ratio characterizes the relative range of the repulsive part of the interatomic potential with respect to the attractive one: the smaller this ratio, the larger the range of the repulsive part with respect to the attractive one. The variation of the surface mismatch as a function of p/q [Eq. (4)] is given in Fig. 2 for the metals listed in Table I.

We see that the largest surface mismatch is obtained for the smallest p/q ratio. This effect can be easily understood from the scheme described in Fig. 3, which depicts in a simplified way the weight of both repulsive and attractive parts for two values of p/q . The creation of a surface results in a loss of a part of both attractive and repulsive interactions. In the case of a small p/q ratio [Fig. 3(a)], the removed repulsive part is larger than the attractive one, which means that at a surface the weight of the attractive part with respect to the repulsive one is larger than in the bulk. Therefore, there is a contraction of the surface lattice parameter. The contraction is weaker in the case of a larger p/q ratio since, in this case, the difference between the removed repulsive part and the attractive one is smaller [Fig. 3(b)].

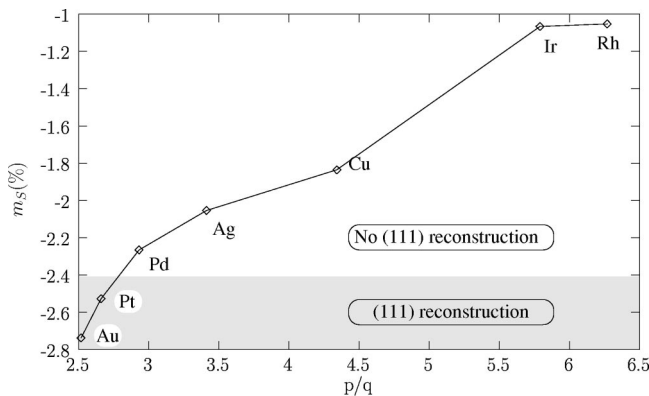


FIG. 2. Evolution of the expected surface mismatch vs the p/q ratio.

The evolution of the p/q ratio for the different metals, leading to smallest values for Pt, and Au, has two origins which are well translated by the TB-SMA model. The first is related to the Thomas-Fermi screening length l_{TF} , which describes the range of the strong electronic forces responsible of the cohesion of metals. l_{TF} varies as $Z^{-1/6}$, where Z is the atomic number.⁴⁵ This means that, when moving from a $3d$ series to a $5d$ series, there is a decrease of l_{TF} ,⁴⁶ inducing a decrease of the range of the attractive part of the interatomic potential. In the framework of the TB-SMA model, this induces an increase of the q parameter, as demonstrated by Spanjaard and Desjonquères.⁴⁷ Such an explanation is in agreement with the one proposed in Ref. 48, which attribute the origin of the reconstruction of the $5d$ metals to the strong relativistic effects in these atoms. Indeed, due to the enhanced concentration of relativistic electrons near the nucleus,⁴⁹ the screening length is reduced when the relativistic effects are strong.⁵⁰

The second origin of the evolution of p/q is related to the d -band filling. Equation (2) gives only the nd -band bonding contribution to the cohesive energy, which increases as the interatomic separation decreases. The stability of the lattice is ensured by the counterbalancing repulsive part [Eq. (3)] which is partly provided by the compression of the free-electron gas, i.e., $(n+1)s$ electrons.⁵¹ The radial extension

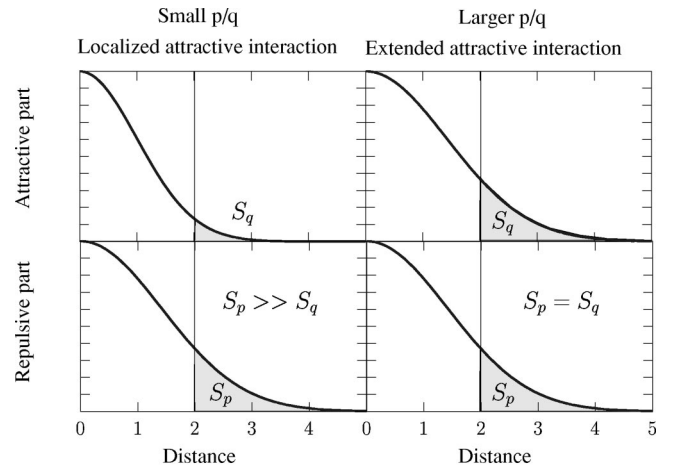


FIG. 3. Schematic view of the range of both the attractive and repulsive parts of the interatomic potential vs the distance from the center of the atom in the case of a small p/q ratio (a) and a larger one (b).

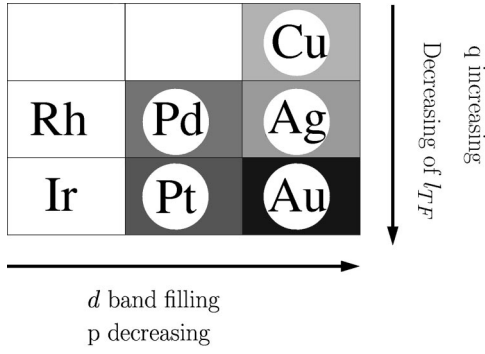


FIG. 4. Variation of the surface mismatch with the position of the element in the Periodic Table. The gray scale corresponds to the surface mismatch values of Fig. 2, and l_{TF} 's the Thomas-Fermi screening length.

of the $(n+1)s$ electrons is larger than that of the nd ones. It means that the more filled the nd band is, the weaker the nuclear charge sensed by the $(n+1)s$ electrons, inducing a spatial extent of the electronic density associated with the $(n+1)s$ electrons. This effect is expressed in an increase of the range of the repulsive part of the interatomic potential when going from the left to the right of the table presented in Fig. 4, meaning a decrease of the p parameter in the framework of the TB-SMA model. The combination of these two effects gives the smaller value of the p/q ratio for elements of the right lower part of Fig. 4, inducing the largest surface mismatch for Au and Pt.

2. Influence of the relative strength of the attractive and repulsive parts of the interatomic potential

The ratio $3A/\xi$ characterizes the strength of the repulsive part of the interatomic potential with respect to the attractive one. From a mathematical point of view, the smaller the $3A/\xi$ ratio, the larger the surface mismatch. The variation of the surface mismatch versus $3A/\xi$ [Eq. (4)] is given in Fig. 5 for the same metals as in Fig. 2. Unlike the p/q dependence, the evolution of the surface mismatch for pure metals does not follow the mathematical evolution of the surface mismatch with respect to $3A/\xi$. This means that the main factor

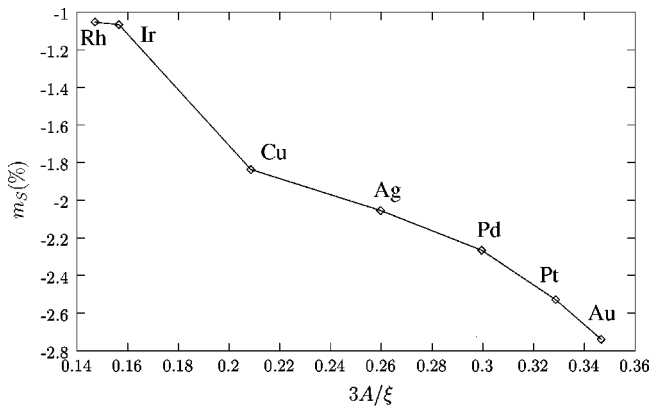


FIG. 5. Evolution of the expected surface mismatch vs the $3A/\xi$ ratio.

influencing the surface mismatch in the metals considered in Table I is the relative range of the repulsive part of the potential with respect of the attractive one, the strength of the repulsive and attractive parts of the potential having nearly no influence.

B. Unidirectional compression of the surface: $22 \times \sqrt{3}$ stripe domain structure

One of the most striking consequence of the surface mismatch is the existence of a stress relief mechanism at the surface of pure metals. From an experimental point of view, the stress relief mechanisms at the (111) surface can be divided in two classes (Fig. 2): (i) Pseudomorphy, when the surface atoms are in registry with the underlying lattice; this is true for elements having a small surface mismatch such as Ag, Pd, Cu, Ir, and Rh. (ii) The formation of discommensuration lines in the surface layer for elements having a large surface mismatch such as Pt (Refs. 2–4) and Au.^{24,52–56} In the case of gold, the local lattice surface parameter is $r_0^s = 2.807 \text{ \AA}$. In the bulk, the surface occupied by one atom in a (111) plane is $S_{\text{atom}} = (\sqrt{3}/2)r_0^2$. This means that for a surface with a local surface lattice parameter r_0^s , there are $N_s = (r_0/r_0^s)^2 \times N_b$ atoms in the surface plane, with N_b the number of atoms in a bulk (111) plane. This corresponds to an increase of about 5% in the number of surface atoms with respect to the bulk ones. However, for gold, the compression of the surface layer is anisotropic, since a compression of about 4.5% is observed experimentally⁵⁴ along the $\langle 1\bar{1}0 \rangle$ direction, while the atoms along the $\langle 11\bar{2} \rangle$ direction stay in registry with the underlying bulk plane. Such an anisotropy cannot be explained by means of the surface stress, since *ab initio* calculations performed on Ir have shown that the surface stress is the same along the $\langle 1\bar{1}0 \rangle$ and $\langle 11\bar{2} \rangle$ directions.⁵⁷ These results are easily transposable to the unreconstructed Au(111) surface. Actually, because the substrate potential is significant, the accommodation between the surface layer and the bulk takes place through the introduction of dislocations. The orientation of these dislocations is determined by the glissile directions. Following Franck's dislocation energy criterion,⁵⁸ the stablest dislocation is given by the smallest norm of the Burgers vector. In the fcc lattice on a (111) plane, the smallest Burgers vector for a perfect dislocation is $\vec{b}_{(1/2)\langle 1\bar{1}0 \rangle} = (1/2)\langle 1\bar{1}0 \rangle$. Then the overclose packing of the surface will be obtained by sliding a part of the surface plane along the $\langle 1\bar{1}0 \rangle$ direction, and by inserting a new atomic row along the $\langle 1\bar{2}1 \rangle$ directions. Nevertheless, there is a low-energy stacking fault in the (111) plane for displacement of $\vec{b}_{(1/6)\langle 1\bar{2}1 \rangle} = (1/6)\langle 1\bar{2}1 \rangle$. This allows a dissociation of the perfect dislocations into two imperfect dislocations with partial Burgers vectors. For instance,⁵⁹

$$\frac{1}{2}\langle 1\bar{1}0 \rangle \Rightarrow \frac{1}{6}\langle 1\bar{2}1 \rangle + \frac{1}{6}\langle 2\bar{1}\bar{1} \rangle. \quad (7)$$

From a structural point of view, the gliding of the half-surface plane along the $\langle 1\bar{1}0 \rangle$ direction involves a larger dilatation, and hence a larger misfit energy than a motion along the $\langle 1\bar{2}1 \rangle$ direction.

Application of the Frank energy criterion shows thus that the elastic strain energy is reduced by the dissociation of the perfect dislocation into partial ones.

$$b_{\langle 1/2 \rangle \langle 1\bar{1}0 \rangle}^2 = a^2 < b_{\langle 1/6 \rangle \langle 1\bar{2}1 \rangle}^2 + b_{\langle 1/6 \rangle \langle 2\bar{1}\bar{1} \rangle}^2 = \frac{2a^2}{3}, \quad (8)$$

where a is the nearest neighbor distance.

Such a decomposition reduces the global dilation of the surface layers by decreasing the in-plane interatomic distances in the core of the dislocation, while keeping the registry of the surface atoms with the bulk lattice. The imperfect dislocations obtained are known as Shockley partial dislocations. From a structural point of view, a Shockley partial dislocation induces a stacking shift of the surface layer from fcc to hcp. The transition area is known as a discommensuration line. Moreover, because decomposition (7) involves two different Shockley partial dislocations, a pairwise arrangement of discommensuration lines exists, the first discommensuration line being related to the fcc \Rightarrow hcp transition while the second one is related to the hcp \Rightarrow fcc transition. Such a pairwise arrangement of discommensuration lines was observed in both homoepitaxial systems [Au(111) (Refs. 24, 55, and 56) and Pt(111) (Refs. 2–4)], and heteroepitaxial ones [Ag/Pt(111) (Ref. 60) and Cu/Ru(0001) (Ref. 61)]. Because of the Franck energy criterion, only one direction of the Burgers vector among the three possible is expected, and hence the whole excess of surface atoms is distributed along a single $\langle 1\bar{1}0 \rangle$ direction. This explains the 4.5% compression along the $\langle 1\bar{1}0 \rangle$ direction, which is in agreement with the 5% of excess surface atoms calculated from the local surface lattice parameter, while the local surface mismatch is only 2.5%.

C. A high-symmetry surface:

The Au(111) herringbone structure

From now on, we restrict our study to the Au(111) surface. A consequence of the stress relief along only one $\langle 1\bar{1}0 \rangle$ direction is to increase the stress along the other two $\langle 1\bar{1}0 \rangle$ directions. Then, because of this threefold orientational degeneracy, the stripe domain reconstruction is unstable for large areas.^{62,63} The best compromise is then the formation of three types of stripe domain reconstructions, each of them associated with one of the three equivalent $\langle 1\bar{1}0 \rangle$ directions. They are separated by a second type of discommensuration line. From a fundamental point of view, this effect is similar to the one which induces the stripe domain reconstruction $22 \times \sqrt{3}$. The intersection between the discommensuration lines of the stripe domain reconstruction and the discommensuration lines associated with the stripe domain reconstruction degeneracy induce the formation of kinks. The kinks are themselves ordered, and produce a structure in which two of three possible rotational equivalent domains of the stripe domain structure alternate periodically across the surface forming the well-known zigzag pattern.^{24,64}

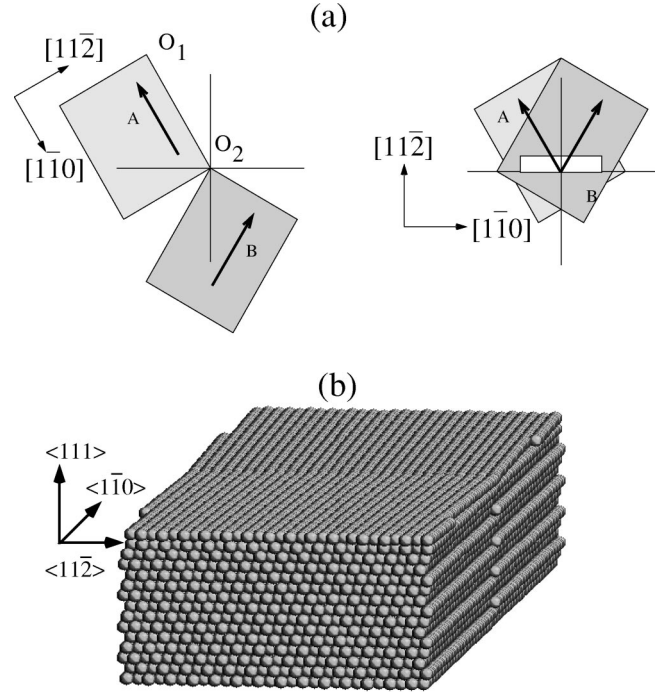


FIG. 6. (a) Scheme of the initial structure building. The black arrow gives the over-close-packing direction. (b) Initial unrelaxed supercell.

III. LOCAL ANALYSIS OF THE Au(111)-RECONSTRUCTED SURFACE

A semi-infinite Au crystal is simulated by means of a finite box subject to periodic boundary conditions along directions parallel to the surface ($\langle 1\bar{1}0 \rangle$ and $\langle 11\bar{2} \rangle$). As we work in the microcanonical ensemble, the number of particles N in each finite box is fixed. This sets a problem for the study of reconstructed surfaces, since reconstruction often implies surface density changes, as mentioned earlier. In real systems extra atoms can be added or removed because reservoirs are present in the form of steps, kinks, or other defects.^{65,66} Such defects are not present in our cell, and the only escape is to adjust the value of the surface atoms number N_S . The choice of the initial structure is based on the experimental observations of the Au(111) surface.^{24,25,55,56}

Thus the first stage consists of proceeding to an overclose packing of the surface along the dense direction $\langle 1\bar{1}0 \rangle$ that is, distributing 23 surface atoms uniformly on 22 bulk atoms. In the perpendicular $\langle 11\bar{2} \rangle$ direction, the atoms are in registry with the bulk. Such a numerical overclose packing is equivalent to an experimental one resulting from an external source such as temperature,^{55,56,67} supersaturation vapor,³ or ion bombardment.⁴ The second stage consists of duplicating the structure described in Sec. II B [the A structure in Fig. 6(a)], and rotating it along the $\langle 111 \rangle$ direction by 120° [the B structure in Fig. 6(a)]. The two structures are then translated in order to superimpose the O_1 and O_2 points. In this way, the bulk lattice of both structures coincide. Only the atoms at $x_{\langle 1\bar{1}0 \rangle} \geq 0$ for structure B and atoms at $x_{\langle 1\bar{1}0 \rangle} < 0$ for structure A are kept. Much attention is required in order to avoid a large overlap between the surface atoms. The final initial

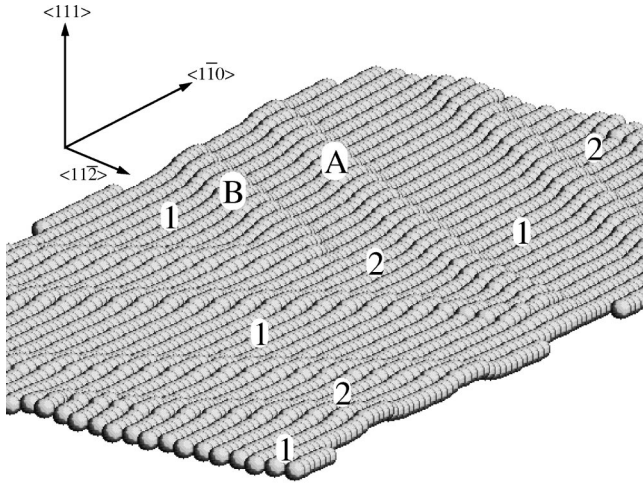


FIG. 7. Part of a 325.44×69.84 -Å² relaxed supercell. Only the first plan is represented. The scale along the $\langle 111 \rangle$ direction (surface normal) has been expanded by a factor 4 in order to amplify the corrugation. See the text.

structure [Fig. 6(b)] is obtained by cutting up a rectangular unit supercell [the white rectangle in Fig. 6(a)].

The relaxation procedure is performed by integrating the equation of motion,⁶⁸

$$\vec{F}_i = m_i \frac{d\vec{v}_i}{dt}, \quad (9)$$

where $v_i(t)$ is the velocity at time t of an atom at site i with mass m_i , and $F_i(t)$ is the force acting on this atom. We use the Verlet algorithm⁶⁹ for the time integration algorithm. A quenching procedure which consists of canceling v_i when the product $F_i(t)v_i(t)$ becomes negative has been applied. The force on the atom at site i is obtained from

$$\vec{F}_i = - \frac{dE_{\text{tot}}}{d\vec{r}_i}, \quad (10)$$

with

$$F_{\text{tot}} = \sum_i E_i^{\text{site}}, \quad (11)$$

where E_i^{site} is the energy of this atom, given by Eq. (1).

Figure 7 represents a topographic view of a part of a 325.44×69.84 -Å² relaxed supercell. The slab consists of 15 (111) bulk planes with one unreconstructed (111) surface plane at the bottom of the slab, and one overclose-packed (111) surface plane. Only this latter is represented. Bulk planes contain 3164 atoms and the reconstructed one contains 3317 atoms, which is equivalent to an average overclose packing of 4.8%. The total number of atoms in the slab is 47613. The scale along the $\langle 111 \rangle$ direction (surface normal) has been dilated by a factor 4 in order to amplify the atomic corrugation. The corrugation around the average position of the atoms in this plane is 0.332 Å. In comparison, the corrugation of the unreconstructed surface is only 0.05 Å. The calculated corrugation is slightly larger than the experimental one [0.20 ± 0.05 Å (Ref. 24)].

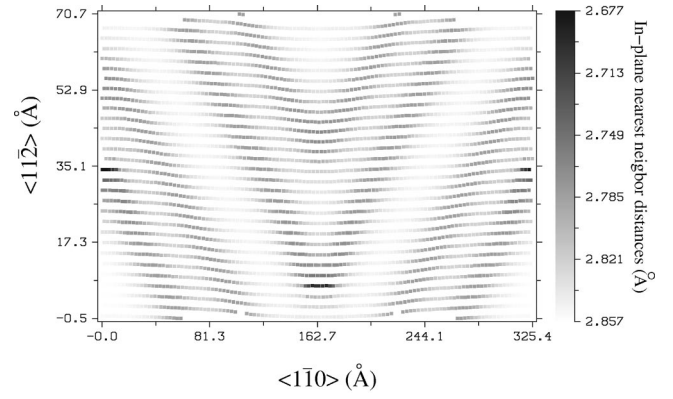


FIG. 8. In-plane nearest-neighbor distances.

The strong structural inhomogeneity of the reconstructed surface is the most remarkable point. Several regions can be observed, as shown in Fig. 8, which displays a map of the mean atomic in-plane nearest neighbor distances. Figure 9 displays the corresponding distribution. In type-1 regions, the surface atoms are nearly in registry with the bulk lattice (2.86 Å). This means that in these regions, the surface lattice keeps the fcc stacking imposed by the bulk lattice. These regions represent about 45% of the surface. Type-2 regions are characterized by a misfit of about 2% (2.82 Å). This latter value is close to the Au(111) surface misfit (Sec. II A). Although this surface lattice constant deviates from the underlying bulk value, because of the small spatial expansion of these regions, the stacking is close to a hcp one with respect to the bulk. These regions account for about 25% of the surface.

A relative misfit of about 5.5% is observed in regions of types A and B, where the mean atomic in-plane nearest-neighbor distances are 2.80 Å in the center of the discommensuration and 2.78 Å on the edge. Regions of types A and B correspond to discommensuration lines, i.e., incommensurate phases. They extend on four atomic sites along the $\langle 1\bar{1}0 \rangle$ direction at the junction between the fcc and hcp areas, and occupy 30% of the surface. Because of the threefold orientational degeneracy, two orientations of the discommensuration lines are present on the surface, making an angle of

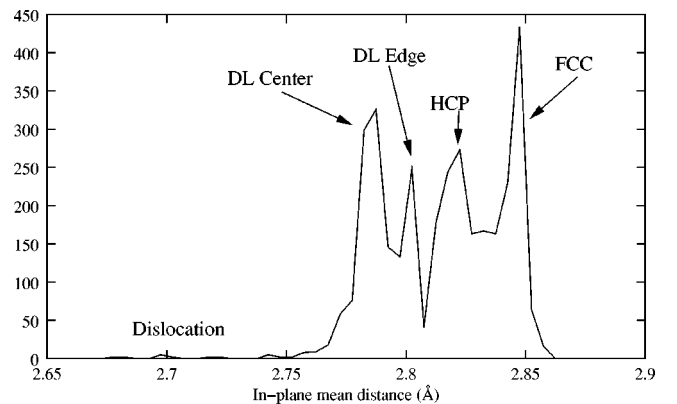


FIG. 9. Distribution of the mean atomic in-plane nearest-neighbor distances. DL is the discommensuration line.

120°. The B discommensuration lines join themselves to form a single continuous partial dislocation between the first and second layers. The A discommensuration lines join themselves through the introduction of an extra atomic row. This description is in agreement with the proposed atomic structure of Ref. 28. In the core of the dislocation, at the junction between the A discommensuration line, the mean atomic in-plane nearest-neighbor distance is 2.68 Å.

The sites of the discommensuration lines have an energy 182 meV higher than the energy of the fcc sites. Moreover, the fcc sites are more stable than the hcp ones, since a difference of 2 meV is calculated. This latter value is coherent with that given by Takeuchi, Chan, and Ho (1.3 meV), obtained from first-principle calculations.⁷⁰

It is worth noting that the calculated surface energy of the herringbone superstructure is slightly higher than the one of the unreconstructed surface: $\gamma_{\text{unrec}} = 0.25$ eV/atom and $\gamma_{\text{rec}} = 0.26$ eV/atom. Therefore, the reconstruction energy E_{rec} defined as the difference $\gamma_{\text{rec}} - \gamma_{\text{unrec}}$ is slightly positive. In this way we have built a substrate less stable than the unreconstructed one because, within our model, it corresponds to a local stable minimum instead of an absolute one. At least the relative site energies of the surface between fcc and hcp sites are well reproduced as well as the topographic corrugation. Nevertheless, the correct geometry of the reconstruction is obtained, provided the relative interaction between the atoms in the surface plane and the interaction between the atoms of the surface and the underlying plane are well described. In addition, we never observe any ejection of atoms from the overfilled surface into adatom positions during the simulations, even upon numerical annealings of the structure. Actually, the most important point is that the Au surface remains reconstructed during all the simulations, which gives a good degree of confidence of our model.

The stress distribution at the gold surface is given in Fig. 10 which displays a map of the local hydrostatic pressure which is defined at $T=0$ K (Refs. 71–73) by

$$P_i = - \frac{dE_i}{d \ln V} = - \frac{1}{3} \text{Tr}[\bar{\sigma}], \quad (12)$$

where V is the atomic volume and $\bar{\sigma}$ is the surface stress tensor. The sign of the stress is given by the sign of P_i : positive for compression and negative for tension. Only the fcc sites are under tension, as in the case of the unreconstructed surface (negative pressure, not shown). This is because these atoms are at the bulk equilibrium distances. Indeed, because of the reduced number of chemical bonds at the surface, they have a lack of electronic density and hence they try to get closer to each other. The pressure in the hcp region is nearly zero, because the distances in this region are close to the surface equilibrium one. The atoms of the discommensuration lines are under compression, with a maximal value at the kink position. This results from the necessity for the system to accommodate two different regions (fcc and hcp) on the surface: locally the situation is unfavorable, but this contributes to a favorable situation for the whole system. Such a surface inhomogeneity of the local hydrostatic pressure allows us to put forward some hypothesis con-

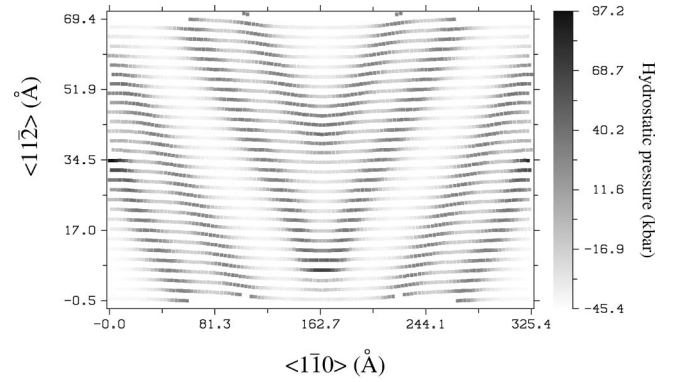


FIG. 10. Distribution of the pressure undergone by the surface atoms.

cerning the adsorption on gold reconstructed surface. From an experimental point of view, it has been reported that some elements such as Co,^{25,26} Fe,²⁷ Ni,^{28,29} Rh,^{30,31} or Cu (Ref. 32) nucleate preferentially at the kinks while some others such as Au (Ref. 74) or Ag (Ref. 75) seem insensitive to the reconstruction. Such a behavior can be explained from atomic size considerations. In the vicinity of the kink, the nearest-neighbor distances are small in order to accommodate the two A discommensuration lines but at the same time it induces a large hydrostatic pressure. Adsorption, and possibly incorporation, of atoms smaller than gold, as for example, cobalt, allow the system to decrease the local hydrostatic pressure by decreasing the equilibrium distance in the kink region, since the equilibrium distance for a Co-Au bond is smaller than the Au-Au one. The addition of a bigger atom would not play in favor of a decreasing pressure in this region (see Fig. 10).

IV. CONCLUSION

In the present work, the behavior of the fcc(111) surface of some metals is studied in the framework of a tight-binding second-moment-approximation model. The concept of *local surface mismatch* is introduced. Such a concept allows one to obtain the local tendency of the surface lattice parameter while taking into account the bonds of the surface atoms with the bulk ones. It is shown that the local surface lattice parameter depends on the relative range of the repulsive part of the potential with respect to the attractive one: the smaller the latter, the greater the local surface lattice mismatch. Conversely, the relative strength of the repulsive part of the potential with respect to the attractive one has no influence.

The consequences of the different strains at surface and in the bulk have been then studied by means of a tight-binding quenched-molecular-dynamics study of the herringbone reconstruction of Au(111). The most striking point is the great inhomogeneity of the mean atomic in-plane nearest-neighbor distances, since a variation from 2.68 to 2.85 Å is obtained. A similar inhomogeneity is observed for the hydrostatic pressure. The fcc sites of the reconstruction are under tension, as in the unreconstructed situation. The hydrostatic pressure is nearly zero in the hcp region. In the discommensuration lines the atoms are under compression. The compression in the

kink region is the most important with a value three times larger than in the discommensuration lines. This high compression is probably at the origin of the preferential nucleation effect of Co, Fe, Ni, Rh, and Cu deposited on a herringbone-reconstructed Au(111) surface. More details about these phenomena will be discussed in a subsequent paper. Adsorption and incorporation on such surfaces is also an issue to investigate. Indeed, in a recent study of the Co adsorption onto a $22 \times \sqrt{3}$ reconstructed Au(111) surface, we have reported the existence of an unexpected adsorption site located on the low-coordinated bridge site on top of the defect lines.⁷⁶ Because of the strong structural inhomogeneity in the kink region, such unexpected adsorption sites could also be present, and hence have a strong influence on the preferential nucleation phenomena. Finally, the concept of local surface mismatch should be transposed to heteroepitaxial systems. It should allow a better prediction of the lattice misfit, which is commonly calculated from the bulk lattice parameter of the adsorbate.

ACKNOWLEDGMENTS

We are grateful to F. Scheurer and J.-P. Deville for helpful discussions.

APPENDIX

The appendix gives the expression of the surface mismatch m_s . These expressions are obtained by considering interactions extended up to the next-nearest neighbors: 12 nearest neighbors $[(x,0,0), (x/2,y,0), (-x/2,y,0), (-x,0,0), (-x/2,-y,0), (x/2,-y,0), (0,2y/3,-z), (-x/2,-y/3,-z), (x/2,-y/3,-z)]$ and three next-nearest neighbors $[(x,2y/3,-z), (-x,2y/3,-z), (0,-4y/3,-z)]$, where x is along the $\langle 1\bar{1}0 \rangle$ direction, y along the $\langle 11\bar{2} \rangle$ direction, and z along the $\langle 111 \rangle$ direction. Six interatomic distances can be then distinguished:

$$\text{Four atoms at } r_1 = \frac{1}{2} \sqrt{x^2 + 4y^2}, \quad (\text{A1})$$

$$\text{Two atoms at } r_2 = x, \quad (\text{A2})$$

$$\text{One atom at } r_3 = \frac{1}{3} \sqrt{4y^2 + 9z^2}, \quad (\text{A3})$$

$$\text{Two atoms at } r_4 = \frac{1}{6} \sqrt{9x^2 + 4y^2 + 36z^2}, \quad (\text{A4})$$

$$\text{Two atoms at } r_5 = \frac{1}{3} \sqrt{9x^2 + 4y^2 + 9z^2}, \quad (\text{A5})$$

$$\text{One atom at } r_6 = \frac{1}{3} \sqrt{16y^2 + 9z^2}. \quad (\text{A6})$$

The surface lattice mismatch is calculated for an isotropic strain. It means that relations exist between x , y , and z : $x = r$, $y = \sqrt{3}/2r$, and $z = \sqrt{2}/3r$, where r is the nearest-neighbor distance. Thus $r_1 = r_2 = r_3 = r_4 = r$ (nine atoms) and $r_5 = r_6 = \sqrt{2}r$ (three atoms). From the Eqs. (1), (2), and (3), the total energy is given by

$$\begin{aligned} E_{\text{tot}} = & -\xi \left\{ 9 \exp \left[-2q \left(\frac{r}{r_0^B} - 1 \right) \right] \right. \\ & + 3 \exp \left[-2q \left(\frac{\sqrt{2}r}{r_0^B} - 1 \right) \right] \left. \right\} + A \left\{ 9 \exp \left[-p \left(\frac{r}{r_0^B} - 1 \right) \right] \right. \\ & + 3 \exp \left[-p \left(\frac{\sqrt{2}r}{r_0^B} - 1 \right) \right] \left. \right\}. \end{aligned} \quad (\text{A7})$$

With the minimization condition

$$\frac{dE}{dr} = 0, \quad (\text{A8})$$

one obtains

$$\begin{aligned} & K \left[3 \exp \left(-p \frac{\delta r}{r_0^B} \right) + \sqrt{2} C_p \exp \left(-\sqrt{2} p \frac{\delta r}{r_0^B} \right) \right] \\ & = \left[3 \exp \left(-2q \frac{\delta r}{r_0^B} \right) + \sqrt{2} C_q \exp \left(-2\sqrt{2} q \frac{\delta r}{r_0^B} \right) \right] \\ & \times \left[3 \exp \left(-2q \frac{\delta r}{r_0^B} \right) + C_q \exp \left(-2\sqrt{2} q \frac{\delta r}{r_0^B} \right) \right]^{-1/2}, \end{aligned} \quad (\text{A9})$$

with

$$C_q = \exp[-2q(\sqrt{2}-1)] \quad (\text{A10})$$

$$C_p = \exp[-p(\sqrt{2}-1)], \quad (\text{A11})$$

$$\frac{\delta r}{r_0^B} = \frac{r}{r_0^B} - 1, \quad (\text{A12})$$

$$K = \frac{\sqrt{3}Ap}{q\xi}. \quad (\text{A13})$$

Because $\delta r/r_0^B \approx 0.01$, one can expand the exponential to first order in $\alpha \delta r/r_0^B$ ($\alpha = -p, -\sqrt{2}p, -2q$, or $-2\sqrt{2}q$):

$$\begin{aligned} & K \sqrt{3 + C_q} \left((3 + \sqrt{2}C_p) - p(3 + 2C_p) \frac{\delta r}{r_0^B} \right) \\ & = \left((3 + \sqrt{2}C_q) - 2q(3 + 2C_q) \frac{\delta r}{r_0^B} \right) \\ & \times \left(1 - 2q \frac{(3 + \sqrt{2}C_q)}{(3 + C_q)} \frac{\delta r}{r_0^B} \right)^{-1/2}. \end{aligned} \quad (\text{A14})$$

Since

$$2q \frac{(3 + \sqrt{2}C_q)}{(3 + C_q)} \ll 1, \quad (\text{A15})$$

$$\left(1 - 2q \frac{(3 + \sqrt{2}C_q)}{(3 + C_q)} \frac{\delta r}{r_0^B}\right)^{-1/2} \approx \left(1 + q \frac{(3 + \sqrt{2}C_q)}{(3 + C_q)} \frac{\delta r}{r_0^B}\right), \quad (\text{A16})$$

and

$$K\sqrt{3 + C_q} \left((3 + \sqrt{2}C_p) - p(3 + 2C_p) \frac{\delta r}{r_0^B} \right) = \left((3 + \sqrt{2}C_q) - 2q(3 + 2C_q) \frac{\delta r}{r_0^B} \right) \left(1 + q \frac{(3 + \sqrt{2}C_q)}{(3 + C_q)} \frac{\delta r}{r_0^B} \right). \quad (\text{A17})$$

To first order in $\delta r/r_0^B$,

$$m_s = \frac{\delta r}{r_0^B} = (3 + C_q) \frac{\sqrt{3}Ap\sqrt{3 + C_q}(3 + \sqrt{2}C_p) - q\xi(3 + \sqrt{2}C_q)}{[\sqrt{3}Ap^2(3 + C_q)^{3/2}(3 + 2C_p) - 2q^2\xi(3 + 2C_q)(3 + C_q) + q^2\xi(3 + \sqrt{2}C_q)^2]}. \quad (\text{A18})$$

*Email address: Herve.Bulou@ipcms.u-strasbg.fr

- ¹L. Pauling, *The Nature of the Chemical Bond* (Cornell University Press, Ithaca, NY, 1960).
- ²D. G. Fedak and N. A. Gjostein, *Acta Metall.* **15**, 827 (1967).
- ³D. Wolf, H. Jagodzinski, and W. Moritz, *Surf. Sci.* **77**, 265 (1978).
- ⁴J. R. Noonan and H. L. Davis, *J. Vac. Sci. Technol.* **16**, 587 (1979).
- ⁵P. Heimann, J. F. van der Veen, and D. E. Eastman, *Solid State Commun.* **38**, 595 (1981).
- ⁶S. H. Overbury, W. Heiland, D. M. Zehner, S. Datz, and R. S. Thoe, *Surf. Sci.* **109**, 239 (1981).
- ⁷L. D. Marks, *Phys. Rev. Lett.* **51**, 1000 (1983).
- ⁸I. K. Robinson, *Phys. Rev. Lett.* **50**, 1145 (1983).
- ⁹H. P. Bonzel and R. Ku, *Surf. Sci.* **33**, 91 (1972).
- ¹⁰H. P. Bonzel and R. Ku, *J. Vac. Sci. Technol.* **9**, 663 (1972).
- ¹¹C. M. Comrie and R. M. Lambert, *J. Chem. Soc., Faraday Trans.* **72**, 1659 (1976).
- ¹²H. P. Bonzel and S. Ferrer, *Surf. Sci.* **118**, L263 (1982).
- ¹³J. C. Campuzano, A. M. Lahee, and G. Jennings, *Surf. Sci.* **152-153**, 68 (1985).
- ¹⁴G. L. Kellogg, *Phys. Rev. Lett.* **55**, 2168 (1985).
- ¹⁵K. Christmann and G. Ertl, *Z. Naturforsch. A* **23a**, 1144 (1973).
- ¹⁶C.-M. Chan, M. A. van Hove, W. H. Weinberg, and E. D. Williams, *Solid State Commun.* **30**, 47 (1979).
- ¹⁷C.-M. Chan, M. A. van Hove, W. H. Weinberg, and E. D. Williams, *Surf. Sci.* **91**, 440 (1980).
- ¹⁸J. D. Wrigley and G. Ehrlich, *Phys. Rev. Lett.* **44**, 661 (1980).
- ¹⁹J. V. Barth, H. Brune, G. Ertl, and R. J. Behm, *Phys. Rev. B* **42**, 9307 (1990).
- ²⁰A. R. Sandy, S. G. J. Mochrie, D. M. Zehner, K. G. Huang, and D. Gibbs, *Phys. Rev. B* **43**, 4667 (1991).
- ²¹A. R. Sandy, S. G. J. Mochrie, D. M. Zehner, G. Grübel, K. G. Huang, and D. Gibbs, *Phys. Rev. Lett.* **68**, 2192 (1992).
- ²²M. Bott, M. Hohage, T. Michely, and G. Comsa, *Phys. Rev. Lett.* **70**, 1489 (1993).
- ²³C. Teichert, M. Hohage, T. Michely, and G. Comsa, *Phys. Rev. Lett.* **72**, 1682 (1994).
- ²⁴J. Jacobsen, K. W. Jacobsen, and P. Stoltze, *Surf. Sci.* **317**, 8 (1994).

- ²⁵S. Narasimhan and D. Vanderbilt, *Phys. Rev. Lett.* **69**, 1564 (1992).
- ²⁶B. Voigtländer, G. Meyer, and N. M. Amer, *Phys. Rev. B* **44**, 10354 (1991).
- ²⁷J. Wollschläger and N. M. Amer, *Surf. Sci.* **277**, 1 (1992).
- ²⁸J. A. Stroscio, D. T. Pierce, R. A. Dragoset, and P. N. First, *J. Vac. Sci. Technol. A* **10**, 1981 (1992).
- ²⁹D. D. Chambliss, R. J. Wilson, and S. Chiang, *J. Vac. Sci. Technol. B* **9**, 933 (1991).
- ³⁰D. D. Chambliss, R. J. Wilson, and S. Chiang, *Phys. Rev. Lett.* **66**, 1721 (1991).
- ³¹E. I. Altman and R. J. Colton, *Surf. Sci.* **304**, L400 (1994).
- ³²I. Chado, F. Scheurer, and J.-P. Bucher, *Phys. Rev. B* **64**, 094410 (2001).
- ³³O. Fruchart (private communication).
- ³⁴C. Herring, *The Physics of Powder Metallurgy* (McGraw-Hill, New York, 1951).
- ³⁵M. Mansfield and R. J. Needs, *J. Phys.: Condens. Matter* **2**, 2361 (1990).
- ³⁶R. C. Cammarata, *Surf. Sci.* **279**, 341 (1992).
- ³⁷R. C. Cammarata, *Prog. Surf. Sci.* **46**, 1 (1994).
- ³⁸B. W. Dodson, *Phys. Rev. Lett.* **60**, 2288 (1998).
- ³⁹J. Friedel, *The Physics of Metals* (Cambridge University Press, Cambridge, 1969).
- ⁴⁰B. Legrand, M. Guillopé, J. S. Luo, and G. Tréglia, *Vacuum* **41**, 311 (1990).
- ⁴¹V. Rosato, M. Guillopé, and B. Legrand, *Philos. Mag.* **59**, 321 (1989).
- ⁴²F. Ducastelle, *J. Phys. (Paris)* **31**, 1055 (1970).
- ⁴³H. Häkkinen, J. Merikoski, and M. Manninen, *J. Phys.: Condens. Matter* **3**, 2755 (1991).
- ⁴⁴M. Guillopé and B. Legrand, *Surf. Sci.* **215**, 577 (1989).
- ⁴⁵I. Meunier, Ph.D. thesis, Université de la Méditerranée (France), 2001.
- ⁴⁶N. W. Ashcroft and N. D. Mermin, *Solid State Physics* (Saunders College Press, Philadelphia, 1975).
- ⁴⁷J. H. Rose, J. R. Smith, F. Guinea, and J. Ferrante, *Phys. Rev. B* **29**, 2963 (1984).
- ⁴⁸D. Spanjaard and M. C. Desjonquères, *Phys. Rev. B* **30**, 4822 (1984).

- ⁴⁹V. Fiorentini, M. Methfessel, and M. Scheffler, Phys. Rev. Lett. **71**, 1051 (1993).
- ⁵⁰J. Ferreirinho, R. Ruffini, and L. Stella, Phys. Lett. **91B**, 314 (1980).
- ⁵¹B. K. Shivamoggi and P. Mulser, Phys. Rev. A **54**, 4830 (1996).
- ⁵²R. P. Gupta, Phys. Rev. B **23**, 6265 (1981).
- ⁵³G. I. Finch, A. G. Quarrel, and H. Wilman, Trans. Faraday Soc. **31**, 1051 (1935).
- ⁵⁴J. Heyraud and J. J. Métois, Surf. Sci. **100**, 519 (1980).
- ⁵⁵U. Harten, A. M. Lahee, J. P. Toennies, and C. Wöll, Phys. Rev. Lett. **54**, 2619 (1985).
- ⁵⁶K. G. Huang, D. Gibbs, D. M. Zehner, A. R. Sandy, and S. G. J. Mochrie, Phys. Rev. Lett. **65**, 3313 (1990).
- ⁵⁷A. Filippetti and V. Fiorentini, Surf. Sci. **377-379**, 112 (1997).
- ⁵⁸F. C. Frank, Physica (Amsterdam) **15**, 131 (1949).
- ⁵⁹J. P. Hirth and J. Lothe, *Theory of Dislocations* (Krieger, Malabar, FL, 1992).
- ⁶⁰H. Brune, H. Röder, C. Boragno, and K. Kern, Phys. Rev. B **49**, 2997 (1994).
- ⁶¹G. O. Pötschke and R. J. Behm, Phys. Rev. B **44**, 1442 (1991).
- ⁶²O. L. Alerhand, D. Vanderbilt, R. D. Meade, and J. D. Joannopoulos, Phys. Rev. Lett. **61**, 1973 (1988).
- ⁶³V. I. Marchenko, Zh. Eksp. Teor. Fiz. **81**, 1141 (1981) [Sov. Phys. JETP **54**, 605 (1981)].
- ⁶⁴C. B. Carter and R. Q. Hwang, Phys. Rev. B **51**, 4730 (1995).
- ⁶⁵M. A. van Hove, R. J. Koestner, P. C. Stair, J. P. Bibérian, L. L. Kesmodel, I. Bartoš, and G. A. Somorjai, Surf. Sci. **103**, 189 (1981).
- ⁶⁶M. A. van Hove, R. J. Koestner, P. C. Stair, J. P. Bibérian, L. L. Kesmodel, I. Bartoš, and G. A. Somorjai, Surf. Sci. **103**, 218 (1981).
- ⁶⁷D. L. Abernathy, D. Gibbs, G. Grübel, K. G. Huang, S. G. J. Mochrie, A. R. Sandy, and D. M. Zehner, Surf. Sci. **283**, 260 (1993).
- ⁶⁸J. B. Gibson, A. N. Goland, M. Milgram, and G. H. Vineyard, Phys. Rev. **120**, 1229 (1960).
- ⁶⁹L. Verlet, Phys. Rev. **159**, 98 (1967).
- ⁷⁰N. Takeuchi, C. T. Chan, and K. M. Ho, Phys. Rev. B **43**, 13 899 (1991).
- ⁷¹V. Vitek and T. Egami, Phys. Status Solidi B **144**, (1987).
- ⁷²P. C. Kelires and J. Tersoff, Phys. Rev. Lett. **63**, 1164 (1989).
- ⁷³G. Tréglia, *Stress and Strain in Epitaxy: Theoretical Concepts, Measurements and Applications*, edited by M. Handbücken and J.-P. Deville (Elsevier, Amsterdam, 2001). An atomistic approach for stress relaxation in materials is shown on pp. 119–150.
- ⁷⁴M. M. Dovek, C. A. Lang, J. Nogami, and C. F. Quate, Phys. Rev. B **40**, 11 973 (1989).
- ⁷⁵C. A. Lang, M. M. Dovek, J. Nogami, and C. F. Quate, Surf. Sci. **224**, L947 (1989).
- ⁷⁶C. Goyhenex and H. Bulou, Phys. Rev. B **63**, 235404 (2001).